Direct Relations between Morphology and Transport in Boolean Models

Christian Scholz,[1, 2] Frank Wirner,[1] Michael Klatt,[3] Daniel Hirneise,[1]
Gerd E. Schröder-Turk,[4, 3] Klaus Mecke,[3] and Clemens Bechinger[1, 5]

[1]*2. Physikalisches Institut, Universität Stuttgart, Pfaffenwaldring 57, 70569 Stuttgart, Germany*
[2]*Institut für Multiskalensimulation, Nägelsbachstraße 49b,*
Friedrich-Alexander Universität Erlangen-Nürnberg, 91052 Erlangen, Germany
[3]*Institut für Theoretische Physik, Friedrich-Alexander Universität Erlangen-Nürnberg, 91058 Erlangen, Germany*
[4]*Murdoch University, School of Engineering & IT, Maths & Stats, Murdoch WA, Australia*
[5]*Max-Planck-Institut für Intelligente Systeme, Heisenbergstraße 3, 70569 Stuttgart, Germany*
(Dated: October 12, 2015)

We study the relation of permeability and morphology for porous structures composed of randomly placed overlapping circular or elliptical grains, so-called Boolean models. Microfluidic experiments and lattice Boltzmann simulations allow us to evaluate a power-law relation between the Euler characteristic of the conducting phase and its permeability. Moreover, this relation is so far only directly applicable to structures composed of overlapping grains where the grain density is known *a priori*. We develop a generalization to arbitrary structures modeled by Boolean models and characterized by Minkowski functionals. This generalization works well for the permeability of the void phase in systems with overlapping grains, but systematic deviations are found if the grain phase is transporting the fluid. In the latter case our analysis reveals a significant dependence on the spatial discretization of the porous structure, in particular the occurrence of single isolated pixels. To link the results to percolation theory we performed Monte-Carlo simulations of the Euler characteristic of the open cluster, which reveals different regimes of applicability for our permeability-morphology relations close to and far away from the percolation threshold.

I. INTRODUCTION

The flow of liquids through porous media is of considerable importance in many scientific areas, such as groundwater pollution, secondary oil recovery or blood perfusion inside the human body [1, 2]. Although the literature on porous media has been growing rapidly over the last decades it is still not fully understood, how transport properties of liquids through porous materials can be related to the microstructure even for single-phase flow. Analytical results exist for regular structures [3], and rigorous bounds have been proposed for random media [4]. Yet, it is still an open question, in particular for many random systems, which structural properties determine the permeability, i.e. the ability of a material to conduct fluid flow.

The permeability k of a porous medium, which is perhaps the most fundamental flow property, relates the flow rate Q and the applied pressure P, according to Darcy's law

$$Q = -\frac{k\,A}{\eta}\nabla P \quad , \tag{1}$$

where A is the cross-sectional area of the material and η the viscosity of the fluid. In Eq. (1) one assumes a linear relation between flow and pressure. This is strictly speaking only valid for low Reynolds number flow (Re < 10) of viscous liquids, where Darcy's law can be derived from the Stokes equation. However, the determination of k still requires the solution of the flow problem on the micro-scale which for many random systems is a humongous computationally expensive task.

For this reason preferably simple relations between geometry and flow in porous media are typically used to predict the permeability. One approach is based on a morphological reconstruction of disordered structures with the help of Boolean models, i.e., structures formed by randomly placed and oriented grains with suitably chosen parameters, which was introduced in [5, 6]. It has been shown, that if a set of morphological quantifiers of the pore space, so-called Minkowski Functionals (MFs), between the original and a reconstructed structure agrees, also the conductivity and elasticity of both materials are similar. Therefore Boolean models are, despite their simplicity, applicable to morphologically describe properties of random porous media, even if the formation process of the original structure might be more complicated. Additionally the question arises whether dynamic quantities, like the permeability, can be directly deduced from the MFs. Such a relation has been proposed in [7], where k has been related to one of the MFs, viz., the Euler characteristic of the conducting cluster in Boolean models of overlapping circles and ellipses. However, this relation requires prior knowledge of the grain density, which might not be available for arbitrary structures. Additionally, other quantities, such as the surface area might influence k [8, 9].

In this article we discuss a generalization to arbitrary microstructures and the range of validity close to and far away from the percolation threshold, which is the highest porosity below which there is no sample-spanning conducting phase. A definition of the effective grain density based on reconstruction schemes via Boolean models

and Minkowski functionals, allows to apply the relation to both phases of Boolean models, i.e., void and grain percolation. However, deviations are found which we attribute to the occurrence or disappearance of individual occupied lattice-sites, which have a significant effect on the topology and, thus, on the effective grain density, without strongly affecting the fluid flow. We find that in the low grain density limit the Euler characteristic's dependence on the porosity is equivalent to the effective medium result for the conductivity. Furthermore numerical results enable us to the determine the range of validity close to the percolation threshold and to link our results to percolation theory.

The paper is organized as follows: In section II, we discuss semi-empirical relations between geometric and transport properties from the established literature. In section III, we explain our microfluidic experiments which allow us to determine flow properties of quasi-two-dimensional (2D) representations of Boolean models. The details of our model structures are explained in section IV and the corresponding Minkowski functionals are discussed in section V. The numerical results of the permeability and conductivity, in particular the validity of the Katz-Thompson model, are addressed in section VI. In section VII, we evaluate our experimental results for void percolation and introduce a power-law relation between Euler characteristic and permeability. We evaluate the possible extension to arbitrary structures, by defining an effective grain number and check its validity for grain percolation. Analytical results for low grain density and computational results close to the percolation threshold are presented in section VIII and IX, which allows us to establish the valid range of our assumption. Finally a summary of the results is presented in section X.

II.   SEMI-EMPIRICAL RELATIONS

Many semi-empirical relations for pressure-driven single phase flow based on the results for flow through regular sphere packings have been proposed [2, 10]. For random porous media, Katz and Thompson proposed a relation between k and the electrical conductivity σ of the fluid saturated phase:

$$k = c\, l_c{}^2 \frac{\sigma}{\sigma_0} \tag{2}$$

where c is a constant that depends on the local pore morphology, σ_0 is the bulk conductivity of the fluid and l_c is a critical pore diameter, equal to the size of the bottle neck of the conducting phase, i.e. the diameter of the largest hard-sphere which can freely penetrate the porous material [11]. Eq. (2) can be derived by using ideas from percolation theory to treat the conductance problem through a porous structure as a percolation problem with a critical threshold value for the conductance and assuming the same critical exponents for the conductance and flow problem. Of course this approach depends on the universality of critical exponents, which might be different

in two and three dimensions and depend for example on the pore size distribution [12–14]. Yet, the validity of Eq. (2) has been shown for various types of natural rock and random media [15–18].

As Eq. (2) relates conductivity and permeability, it is typically called a cross-property relation to distinguish it from a purely geometrical relation to transport properties. The ratio of the bulk conductivity of the fluid σ_0 to the effective conductivity of the porous medium saturated with that fluid σ is called formation factor

$$F = \frac{\sigma_0}{\sigma} \quad . \tag{3}$$

For many random porous media it is assumed that F is related to the porosity ϕ, i.e., the volume fraction of the conducting phase, by Archie's law

$$\frac{\sigma}{\sigma_0} = \left(\frac{\phi - \phi_c}{1 - \phi_c} \right)^{\mu} \quad , \tag{4}$$

where ϕ_c is the percolation threshold [19, 20], i.e., the porosity at which the type of porous material ceases to percolate and μ is an exponent, which typically depends on the porosity and morphology, but might be associated with the critical conductivity exponent close to ϕ_c, where it is expected to be universal and $\mu \approx 1.3$ in 2D [12, 21–24].

Two issues that limit the applicability of Eq. (4): (1) according to percolation theory, Eq. (4) is only valid close to ϕ_c and (2) ϕ_c is a parameter which explicitly depends on the formation process of a structure and cannot be deduced from single finite realizations of this process [25, 26]. Astonishingly, even for simple formation processes, such as percolation on a lattice or continuum percolation of overlapping grains, ϕ_c is not known analytically. To resolve these two issues, a relation independent of ϕ_c is required to accurately predict σ and k of arbitrary finite-sized porous media.

III.   EXPERIMENTAL METHODS

We create micro-model structures for the experimental determination of the permeability using the well-established soft-lithography method [27, 28]. The samples consist of three separated rectangular channels of height h on the order of $10\,\mu\text{m}$, which are connected to pressure reservoirs (see Fig. 1 (a) and (b)). Each channel has a length on the order of 10 mm and a width of 3.5 mm. A porous structure of length $L_{\text{struct}} = 3.5$ mm is placed in the center of the middle channel. The two outer channels contain no porous structures, except for a diluted array of supporting pillars of diameter $10\,\mu\text{m}$ with typical spacing of $500\,\mu\text{m}$ ($\phi > 0.999$). A dilute suspension of colloidal particles of diameter $\sigma = 3\,\mu\text{m}$ is injected into this microfluidic device as tracer particles. For macroscopic experiments the permeability according to Eq. (1) is typically determined by applying a fixed flow rate and then measuring the pressure drop across the

porous structure. However, for soft-lithographic channels to prevent feedback and leakage, only small flow rates must be applied, which requires high-sensitivity motorized syringes. Additionally, an accurate determination of the pressure drop between inlet and outlet is required, which is difficult to achieve with macroscopic pressure transducers.

For this reason we use particle tracking velocimetry [29–31] to determine the average velocity of the injected colloidal tracer particles as a function of the applied pressure ΔP in each channel. Here, in contrast to the fixed flow-rate method, the applied hydrostatic pressure can be tuned accurately by varying the water level in the two reservoirs. The outer channels act as references to calibrate the relationship between particle velocity and fluid velocity. As shown in previous experiments [32–34], the average particle speed within thin rectangular channels typically deviates significantly from the average fluid velocity, depending on the particle diameter, the height of the channel and the particles' gravitational height [35, 36]. However, the mean fluid velocity $\bar{v}$ and mean particle velocity $\bar{u}$ in a channel are proportional [37], so that

$$\bar{v} = c_d \bar{u}\,. \tag{5}$$

The fluid flow problem in the reference channels, which are assumed to be infinite parallel plates, can be solved analytically for a given pressure drop ΔP. The permeability k_0 of the reference channels is equal to $h^2/12$ [38]. Therefore, the calibration factor c_d can be obtained by calculating the theoretical value for $\bar{v}$ with Eq. (1) and measuring $\bar{u}$. Since $k_0 \propto h^2$, the calibration is very sensitive to the height of the structure (and its spatial variations) [38]. We doublecheck the calibration for each sample with two reference channels to account for differences between individual samples, which can occur during the lithographic process. Fig. 1 (c) shows an exemplary plot of $\bar{u}$ vs. ΔP for the three channels of one sample. As illustrated, the fluid velocity in the channel containing the porous structure is considerably slower, while in the reference channels it is similar (small differences are caused by the different length ($\Delta L \approx 500\,\mu\mathrm{m}$) and slightly different height of the channels ($\Delta h \approx 0.5\,\mu\mathrm{m}$), which result from the production process).

By considering the middle channel as a series of hydraulic resistances $R_{hyd} = \frac{\Delta P}{Q}$, as depicted in the equivalent circuit diagram in Fig. 1(b), we can determine the permeability of the central structure directly from the flow rate. If all flow rates are known, the relative permeability (normalized to the k_0 of the reference channel) of a structure is given by

$$\frac{k_{\mathrm{struct}}}{k_0} = \frac{L_{\mathrm{struct}}}{L_{\mathrm{ref}}\frac{Q_{\mathrm{ref}}}{Q_{\mathrm{struct}}} - (L_{\mathrm{in}} + L_{\mathrm{out}})}\,, \tag{6}$$

where L_{ref} is the total length of the reference channel and $L_{\mathrm{in/out}}$ are the length of the inlet and outlet of the structure channel (see Fig. 1(a)).
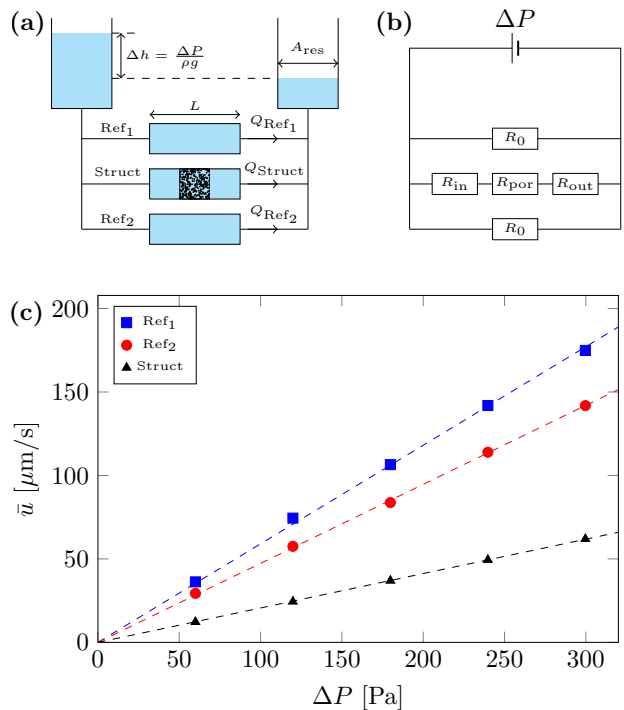

FIG. 1. (Color online) Summary of experimental method: **(a)** A microfluidic sample with a porous structure in the center of the middle channel is created. A dilute suspension of colloidal particles is injected into the device and an external hydrostatic pressure is applied with the help of two reservoirs. The flow rate through the channel is measured from the velocity of the colloidal tracers. Unpatterned reference channels for calibration are added parallel to the structured channel. To account for possible deviations in the channel height two reference channels are used to cross-check the results. **(b)** Equivalent circuit diagram of hydraulic resistances $R_{hyd} = \frac{\Delta P}{Q} = \frac{\eta L}{kA}$. **(c)** Mean particle velocity $\bar{u}$ measured in the two reference and the middle channel containing the porous structure as a function of the applied pressure. The dashed lines are fits to the data points. The average particle velocity $\bar{u}$ is lower in the structured channel due to the lower permeability of the porous part. The fluid velocity in the structure channel is noticable slower than in the reference channels. Similar fluid velocities are found in the reference channels, however differences are caused by different length ($\Delta L \approx 500\,\mu\mathrm{m}$) and height ($\Delta h \approx 0.5\,\mu\mathrm{m}$) of the reference channels and must be taken into account. The error bars are smaller than the symbol sizes.

From Eq. (5) we have $Q_{\mathrm{ref/struct}} = c_d \cdot \bar{u}_{\mathrm{ref/struct}} \cdot A$, which allows us to directly determine the permeability from a parallel measurement of $\bar{u}$ in the reference and structure channels. It is important to note, that crossover effects between the different sections of the middle channel are neglected here, i.e., the individual segments are assumed to be well-connected.
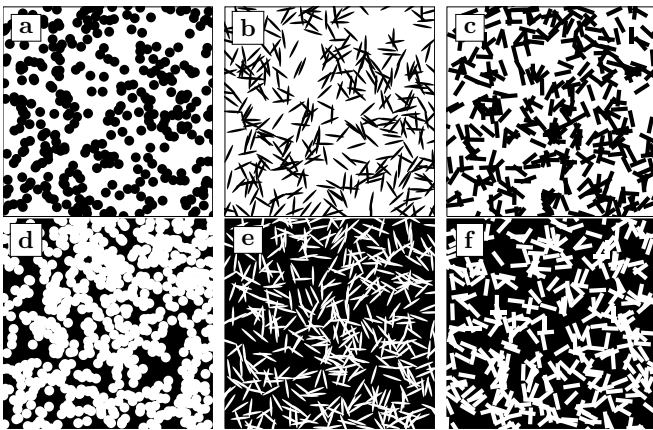
FIG. 2. Boolean models of overlapping grains for **(a)** circles, **(b)** ellipses and **(c)** rectangles. A set of N points is selected randomly in a plane (total area L^2) (Poisson process). At each point a grain with random orientation is placed. Each structure is characterized by its point density N/L^2. The white phase corresponds to the conducting phase. (a)-(c) are structures which we classify as void percolation, whereas the structures (d)-(f) exhibit grain percolation.
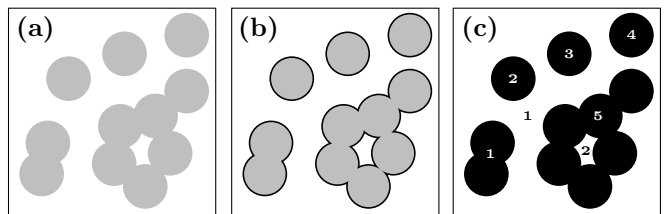

FIG. 3. Schematic illustration of the Minkowski functionals: **(a)** The area V of the conducting phase is shown in white, **(b)** the perimeter P corresponds to the length of the black boundary, and **(c)** the Euler characteristic χ is the number difference of the connected components of each phase, which in the case shown would be $2 - 5 = -3$. The open Euler characteristic χ_o (similar to open porosity ϕ_o and open perimeter S_o) does not count any inclusions, i.e. $\chi_o = 1 - 5 = -4$, as the inclusion in cluster no. 5 would be neglected.

IV. BOOLEAN MODELS

Boolean Models are well established models for porous materials from stochastic geometry [39–41]. There, porous structures are composed of overlapping grains with random position and orientation (i.e., points in a plane are chosen randomly in a Poisson point process). At each point a grain is placed and in the case of anisotropic grains orientations are also chosen randomly from a uniform distribution. In this article, we consider models of randomly overlapping monodisperse circles (ROMC) and randomly overlapping monodisperse ellipses (ROME) with isotropic random orientation. We also simulate systems of overlapping monodisperse rectangles (ROMR) with random orientation, which allows us to minimize discretization errors, because such grains can be, in contrast to spheres, directly represented by polygons of arbitrary precision. Each structure is parametrized by the type, aspect ratio and number N or number density $\rho = N/L^2$ of grains, where L is the linear system size. Examples of these models are shown in Fig. 2 for grain percolation (a)-(c) and void percolation (d)-(e). The white phase corresponds to the conducting phase. Exchanging the two phases results in totally different pore space morphologies. For the experimental and numerical determination of conductivity and permeability, we create five realizations of ROMC and ROME structures on a quadratic 2D-lattice with linear size $L = 4000$ in pairs of equal open porosity ϕ_o, i.e., the volume fraction of only the sample-spanning part of the conducting phase. The circles have a radius of $r = 34$ in units of lattice sites and the ellipses have a long and short semi-axis of $a = 96$ and $b = 12$. In the microfluidic samples this equals $r \simeq 30\,\mu$m and $a \simeq 84\,\mu$m. The mor-

phological properties of the resulting structures and their percolating phase (marked with an index o) are summarized in Table I.

V. MINKOWSKI FUNCTIONALS

Minkowski functionals are morphological measures, corresponding to volume and surface integrals of geometric sets, which are particularly useful for characterizing random structures [39, 42–47]. In two dimensions (2D) the Minkowski functionals of a compact set $\mathfrak{A}$ are given by

$$W_0(\mathfrak{A}) = \int_{\mathfrak{A}} d^2\boldsymbol{r} \quad , \tag{7}$$

$$W_1(\mathfrak{A}) = \frac{1}{2} \int_{\partial\mathfrak{A}} d\boldsymbol{r} \quad , \tag{8}$$

$$W_2(\mathfrak{A}) = \frac{1}{2} \int_{\partial\mathfrak{A}} \frac{1}{R} d\boldsymbol{r} \quad , \tag{9}$$

where R is the local curvature. From this definition, the MF in the continuum can be identified with area V, perimeter P and Euler characteristic χ of a set: $V = W_0$, $P = 2W_1$, and $\chi = W_2/\pi$, so that the values for a unit disk are $W_i = \pi$. On a 2D lattice the normalization of W_i is chosen differently, so that the values for a unit pixel are $W_i = 1$, i.e., $V = W_0$, $P = 4W_1$, and $\chi = W_2$.

The Euler characteristic is a topological constant, which in 2D is equivalent to the number difference between connected components and holes in a set. This quantitiy is particularly useful for the characterization of percolating structures, because for many random sets, χ becomes zero close to the percolation threshold, i.e. the number of connected components of both phases are approximately the same.

For Boolean models in the continuum the MFs of indi-

vidual grains (local MFs w_i) and the mean MFs of realizations of the model (global MFs W_i) with mean density $\rho = \langle N \rangle / L^2$ are related by

$$W_0(\rho)/L^2 = 1 - e^{-\rho w_0}, \tag{10}$$

$$W_1(\rho)/L^2 = \rho w_1 e^{-\rho w_0}, \tag{11}$$

$$W_2(\rho)/L^2 = \rho \left(w_2 - \frac{(2w_1)^2}{4} \rho \right) e^{-\rho w_0}. \tag{12}$$

However, porous structures, in particular when obtained from experimental data are often represented as discretized binary datasets on a lattice. For such data it is convenient to define the MFs in a discrete system. For Boolean Models on a lattice with 8-point connectivity (horizontal,vertical and diagonal neighbors) the relations are

$$W_0(\rho)/L^2 = 1 - e^{-\rho w_0}, \tag{13}$$

$$W_1(\rho)/L^2 = e^{-\rho w_0} \left(1 - e^{-\rho w_1} \right), \tag{14}$$

$$W_2(\rho)/L^2 = e^{-\rho w_0} \left(-1 + 2e^{-\rho w_1} - e^{-\rho(2w_1 + w_2)} \right). \tag{15}$$

In both cases these equations are invertible. Such an inversion has been used to determine Boolean Models with grain compositions with matching w_i to reconstruct natural porous media, such as Fontainebleau sandstone [5]. Numerically the Minkowski functionals can also be calculated for the percolating (open) phase. From this we obtain ϕ_o, S_o and χ_o.

VI. KATZ-THOMPSON MODEL

In the literature it is controversially discussed whether permeability and conductivity have different or equal scaling exponents [2]. In the Katz-Thompson model equal scaling exponents are assumed, which gives a relationship between conductivity and permeability based on arguments from percolation theory. This equality is relevant in our case, since many analytical results on the pore scale are only obtained for the conductivity, but not the permeability of porous media.

The length scale which determines the permeability in the Katz-Thompson model is identified as the critical pore diameter (see Fig. 4(b)). Due to the quasi 2D geometry of our samples this critical diameter is given by

$$l_c = \min(D_c, h) \quad , \tag{16}$$

where D_c is the actual 2D critical diameter. If this diameter is greater than the height h of the structure, h confines the flow and becomes the relevant length scale. For our structures we determined l_c directly from the images of the structures computing the Euclidean distance transform (EDT). For each point in the conducting phase of the sample the EDT assigns the distance to the closest point on the surface. From this l_c can be easily identified
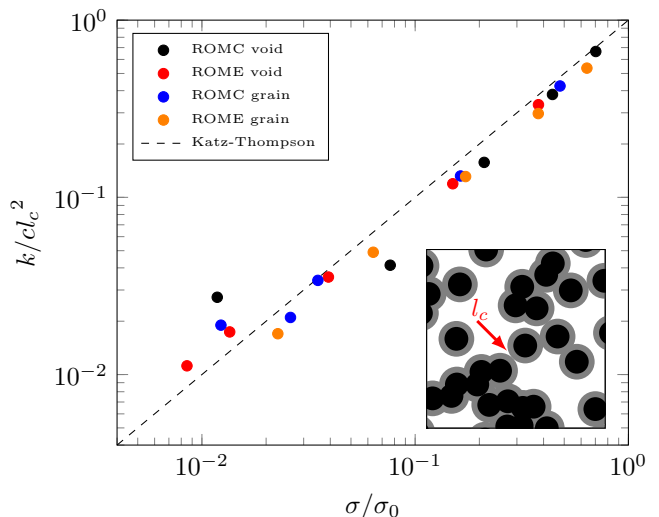

FIG. 4. (Color online) Cross-property relation between permeability k determined by LB simulations and conductivity σ obtained from FEM simulations. The conductivity is normalized by the bulk conductivity σ_0. The permeability is normalized by the square of the critical pore diameter l_c and a constant $c = 1/12$, determined from the limit $l_c \to h$ and $\phi \to 1$, where the system equals the flow problem between infinitely large parallel plates with spacing l_c. Inset: Determination of the critical pore diameter l_c from parallel surfaces.

[48, 49] (see inset of Fig. 4). The constant $c = 1/12$ is chosen to fit the dilute grain limit, where $c l_c^2 = h^2/12$.

In Fig. 4 the relative permeability is shown in dependence of the conductivity, both determined numerically from lattice-Boltzmann (LB) and finite-element (FEM) simulations, respectively. The prediction of the Katz-Thompson model is depicted as a dashed line. In particular for larger ϕ, the data agrees very well with the Katz-Thompson model, with only a slight deviation of the permeability towards lower values than predicted. Additionally even for low permeabilities the predictions deviates by less than a factor of two for all but one structure.

For $\phi \to 1$, this agreement is not surprising, since the height of the structure is much smaller than the distance between the obstacles, which leads to an equivalence of the flow and the conductance problem since the weight of the different pathways is the same for flow and conductance. As the flow profile is locally equivalent to flow confined between infinitely large parallel plates the system can be thought of as a network of hydraulic conductors with conductivity proportional to h^3. In both cases, a homogeneous current or flow is only disturbed by isolated obstacles, which only locally influences the (hydraulic) conductance of the porous structure, without changing the hydraulic radius, which remains on the order of the height h.

However, this is not the case close to the percolation threshold ϕ_c. Katz and Thompson argue, that σ and k

follow similar universal power-laws close to the critical porosity, with an accurate choice of the critical pore diameter. According to some authors this is only true for two-dimensions [12–14]. Otherwise non-universal power-law exponents have to be considered. To obtain further insight into this problem we show the current density and the flow velocity magnitude for representative ROMC and ROME structures in Fig. 6. Even though the fields share some morphological features, such as the principal flow paths, the decay of the current magnitude into dead ends appears to be faster than that of the fluid velocity. This feature is also observed when considering the distribution of currents or flow velocity respectively. As shown in Fig. 8 the current distribution decays faster for both structures. However, the distributions appear to be qualitatively similar, which could explain the surprisingly accurate prediction of the Katz-Thompson conjecture.

VII. TRANSPORT AND MORPHOLOGY

Transport in Boolean models is either described by percolation theory or by effective medium approximations [22]. In percolation theory one assumes that close to ϕ_c transport properties are described by power-laws and far away from ϕ_c effective medium theories are applied. In both cases the data agrees qualitatively with this assumption. In Fig. 5 both the experimentally (closed symbols) and numerically obtained values (open symbols) for the permeabilities k are plotted versus several quantities for void and grain percolation. As shown in Fig. 5(a) and Fig. 5(b) the permeabilities vanish close to ϕ_c and approach the value of an unpatterned channel for $\phi \to 1$. Due to the finite size of the samples the measured permeabilities scatter more and more as the percolation threshold is approached. Due to the finite system size some structures have porosities below ϕ_c and are still conductive (technically for these models ϕ_c is only well-defined for infinite systems). This becomes particularly clear when k is plotted vs. the rescaled porosity (see Fig. 5(c),(d)), as motivated by Archie's law. The measured permeabilities collapse onto a single curve within the experimental accuracy. However in the case of negative rescaled porosities, Eq. (4) obviously cannot be applied. In dependence of the open porosity for void percolation, ROMC structures have a higher permeability than ROME structures for equal ϕ_o (see Fig. 5(e)). In the case of grain percolation this situation is reversed (see Fig. 5(f)). This fact can be explained from the morphology of the velocity fields as shown below. Compared to circles the ellipses form more elongated interconnected obstacles with a significant amount of stagnant parts between grains. This reduces the permeability significantly. In the case of grain percolation the ellipses form more direct pathways for the flow which explains the higher permeability compared to ROMC structures. The ex-

perimental and numerical results support that

$$k = c l_c{}^2 \left(\frac{1 - \chi_o}{N} \right)^\alpha \qquad (17)$$

for the void percolation models [7] where α is a free parameter. Eq. (17) can be justified from the velocity magnitude distributions inside the porous structures shown in Fig. 6. When comparing ROMC and ROME structures it becomes clear that circular grains form more compact obstacles at equal ϕ_o compared to elliptical grains (compare (Fig. 6(e)) and (Fig. 6(f))), because the probability to overlap, and form more tortuous pathways as well as dead ends where no flow occurs, is larger for elongated ellipses at equal grain densities. This fact is captured by the factor $(1 - \chi_o)/N$, which can be interpreted as the number density of obstacles formed by joined grains. All data points for void percolation are well-described by a fit to Eq. (17) with $\alpha_v = 1.27$ (see Fig. 5(g)), which is close to the critical exponent $\mu = 1.3$ in 2D for Archie's law.

One particular shortcoming of Eq. (17) is the explicit dependence on the grain number N, which might be unknown or ill-defined for many porous materials, where the formation process is unknown. Also in the case of grain percolation, the use of N in the denominator of Eq. (17) gives even the wrong limit $k = 0$ for $N \to \infty$. Therefore we replace N by an effective grain number $\hat{N}$, which is derived from the morphological correlations of the Minkowski functionals of Boolean models (Eq. (10)-(12)). In the continuum one obtains

$$\hat{N} = \frac{P^2}{4\pi A \phi} - \frac{\chi}{\phi} \qquad (18)$$

and from (13)-(15) on the 2D lattice

$$\hat{N} = -L^2 \cdot \ln\left(\frac{\chi}{L^2 \phi} \left(1 - \frac{S}{4L^2 \phi} \right)^{-2} \right) - \left(1 - \frac{S}{4L^2 \phi} \right)^{-2} + 2 \left(1 - \frac{S}{4L^2 \phi} \right)^{-1} . \qquad (19)$$

In the case of void percolation $\hat{N}$ is, as expected, typically close to the actual value of N (see Tab. I). In this case $\hat{N}$ can either be calculated from vectorized images (the binary images of the structures are vectorized using a marching squares algorithm) using Eq. (18) or directly from the raster images using Eq. (19). As shown in Tab. I, similar values are obtained, with slightly better agreement of $\hat{N}$ and N for the lattice equation. For grain percolation the role of both phases is inverted and $\hat{N}$ does obviously not correspond to N, but instead is used to define an effective grain number. As shown in Fig. 5(h) the prediction of the permeability, i.e., the black dashed line which we got for void percolation, is quite accurate for ROME structures at high porosities, but significantly overestimates k for ROMC structures. The reason for this deviation might be the occurrence of
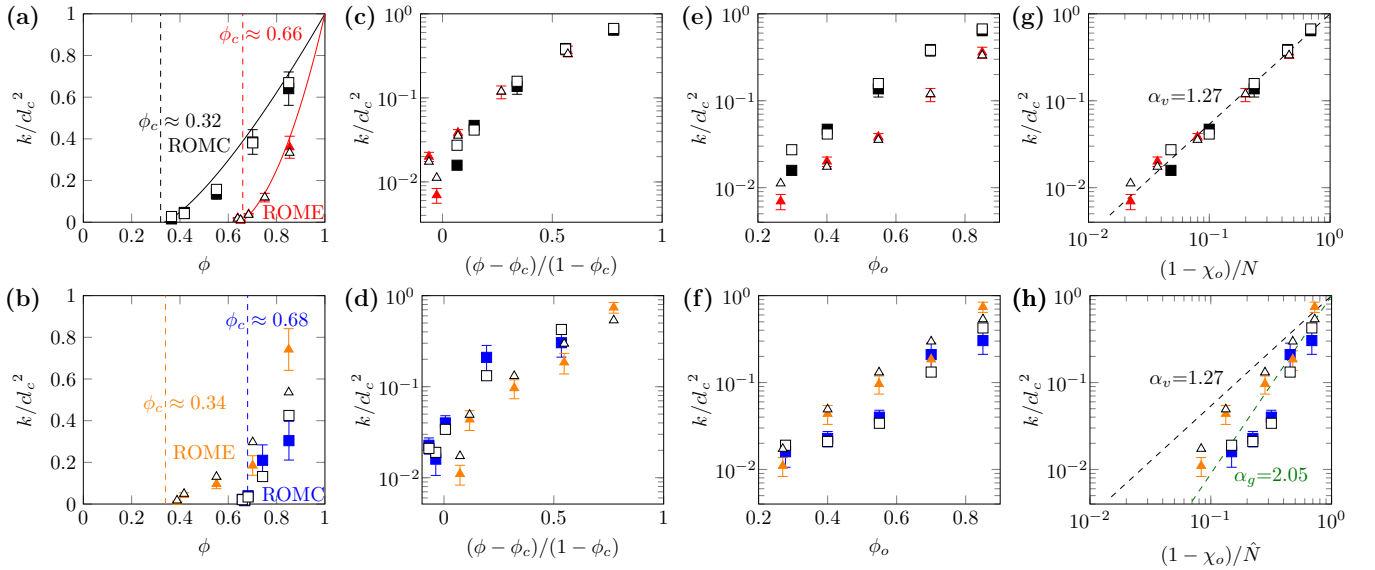
FIG. 5. Experimentally (closed symbols) and numerically (open symbols) determined permeability k of void (top) and grain percolation (bottom) vs. different morphological properties: (a),(b) Porosity ϕ: As expected $k/c\,l_c^2$ vanishes around ϕ_c and goes to 1 for $\phi \to 1$, (c),(d) rescaled Porosity: Data points collapse with some deviations due to finite-size effects, (e),(f) open porosity: for void percolation ROMC structures have higher permeabilities, for grain percolation ROME structures have higher permeability at equal ϕ_o and (g),(h) Euler characteristic: data collapses onto a single curve for void percolation, but for grain percolation deviations are found. The dashed lines in (g) and (h) are fits to Eq. (17) with one free parameter α. Error bars are only shown if larger than symbol size.

many very small isolated obstacles (see Fig. 7) with a size of a few pixel, which significantly influence $\hat{N}$ without strongly influencing k. Such isolated obstacles are found more frequently for ROME than for ROMC structures. Looking again at Fig. 5(h), the data points follow a similar trend as in Fig. 5(g). However, the scattering is significantly stronger. A fit of Eq. (17) to the measured data, which is shown as green dashed line, yields an exponent $\alpha_g = 2.05$. The quantitative deviation from α_v could indicate that the motivation which gave rise to Eq. (17) is obviously not directly applicable in the case of $\hat{N}$ for arbitrary structures. The factor $(1-\chi_o)/N$ was interpreted as the number density of obstacles which are formed by joined individual grains. This interpretation is not that straightforward for grain percolation, since the obstacles are formed by what is left after removing a number N of circular or elliptical areas. However, even in this case the equation does not fail qualitatively, so that we expect a reasonable prediction of k for any structures composed of overlapping grains.

VIII. LOW GRAIN DENSITY

The success of the relation (Eq. (17)) between permeability and Euler characteristic of Boolean models raises the question whether certain results can be obtained analytically or at least semi-empirically. In the regime of low grain density analytical results are available for the conductivity σ [51]. In this regime, i.e., for $\phi \to 1$ the Euler

characteristic of the conducting phase becomes $\chi_o \to \chi$ as the grain density is so low that individual grains do not overlap. Consequently we can expand Eq. (10)-(12) and obtain

$$-\frac{\chi}{N} = 1 - \left(1 + \frac{(4aE(1-\frac{b^2}{a^2}))^2}{4\pi^2 ab}\right)(1-\phi) + \mathcal{O}(\phi^2)\,, \tag{20}$$

where a and b are the long and short semi-axis of the ellipse and E is the elliptical integral of the second kind. Here we approximate the circumference of the ellipse $4aE(1-\frac{b^2}{a^2}) \approx \pi\sqrt{2(a^2+b^2)}$ and obtain

$$-\frac{\chi}{N} \approx 1 - \frac{(a+b)^2}{2ab}(1-\phi)\,. \tag{21}$$

This result is indeed equivalent to the exact result for σ of a conductive sheet with a small number of circular obstacles (i.e. the dilute limit) in 2D [51] and thus

$$\frac{\sigma}{\sigma_0} \approx -\frac{\chi}{N}\quad. \tag{22}$$

For large obstacle densities however, no analytical results are available. In the region close to ϕ_c, where Boolean models fall into the universality class of 2D lattice percolation, it is assumed that the conductivity is described by power-laws, as previously stated [22]. However, whether the same is true for χ_o is not obvious. In the following we present a numerical analysis of the dependence of χ_o close to ϕ_c, in the intermediate range and far away
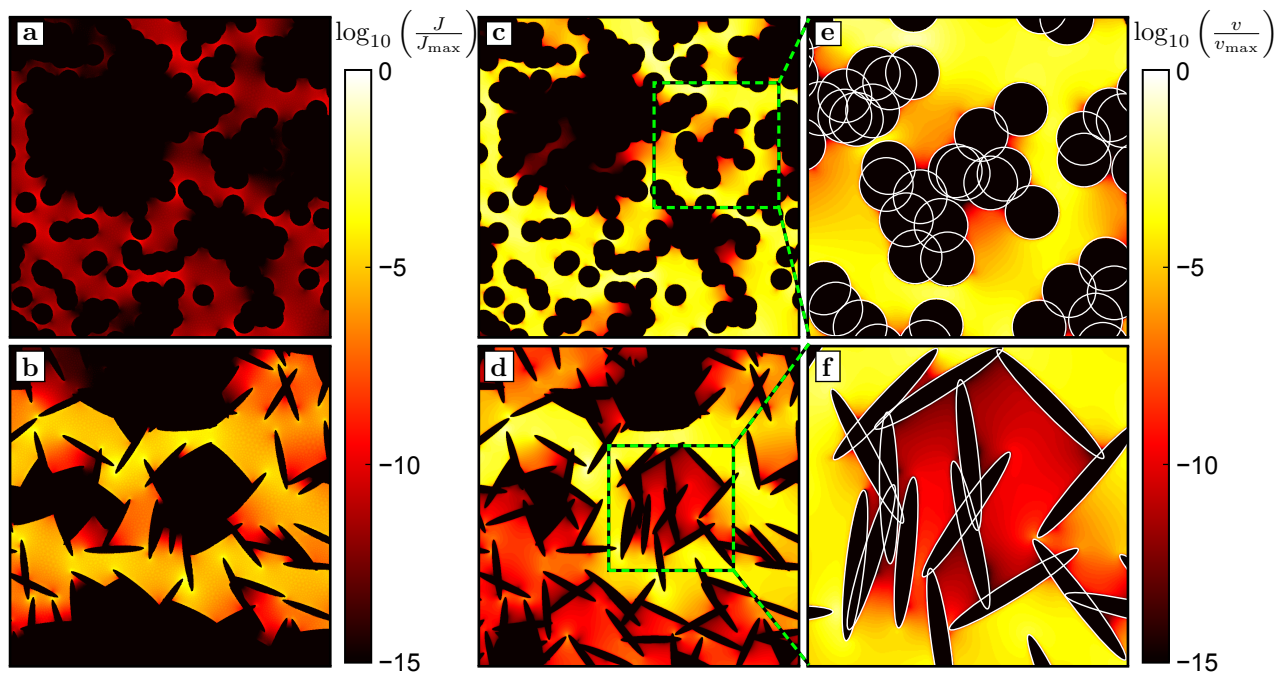
FIG. 6. (Color online) **(a)**,**(b)** Current density magnitude from finite-element simulations of the Laplace equation (i.e. conductivity) normalized to the total maximum current. **(c)**,**(d)** Fluid velocity magnitude from lattice-Boltzmann simulations. For elliptical grains the overlap leads to pronounced stagnant parts, while circular grains form more compact obstacles, as illustrated in **(e)**,**(f)** respectively. Within such stagnant parts a strong decrease of both the current and the flow velocity is observed. However the decrease of j appears to be faster, as observed in [50].
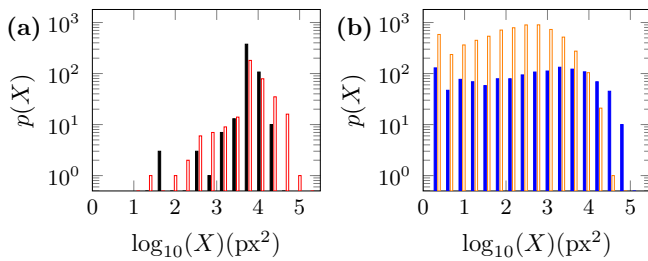

FIG. 7. (Color online) Distribution for obstacle sizes $p(X)$ for void percolation **(a)** and grain percolation **(b)**. Open bars correspond to ROME and filled bars correspond to ROMC structures. The histograms for grain percolation show a large number of very small obstacles.

from ϕ_c for Boolean models and lattice percolation, in dependence of grain shape and system size, to evaluate the possible universal behavior of χ_o and link the results to percolation theory.

IX. CRITICAL BEHAVIOR

Close to ϕ_c transport properties can change dramatically, due to the fractal behavior of the percolating cluster. Results can then depend dramatically on the system

size. In percolation theory a universal critical exponent is assumed for the conductivity. Because of the relation between ϕ_c and χ_o in Eq. (17), the question arises whether χ_o also shows a critical behavior close to ϕ_c. To analyze the dependence of χ_o on the system size and ϕ close to ϕ_c we generate two different types of structures that minimize discretization errors: site percolation on a lattice and ROMR structures in the continuum.

The percolation probability of site percolation systems close to ϕ_c is described by a universal exponent $\beta = 5/36$ which is known analytically in two dimensions from conformal field theory (we use the standard notation for critical exponents as common in the literature, e.g. [26]). Boolean models of randomly overlapping grains fall into the same universality class, so the critical exponents are equal. However, the percolation threshold is non-universal and depends on the details of the grains.

In the case of the Euler characteristic the problem is less well understood. Although for many random fields the Euler characteristic can be determined analytically, this is not the case for the Euler characteristic of the open phase, i.e., the percolating cluster. For fractals, the scaling of area, perimeter and Euler characteristic behave differently. While the area scales with one critical exponent, such as in the case of the percolation probability, the perimeter has one additional, and the Euler characteristic has two additional scaling exponents, which are
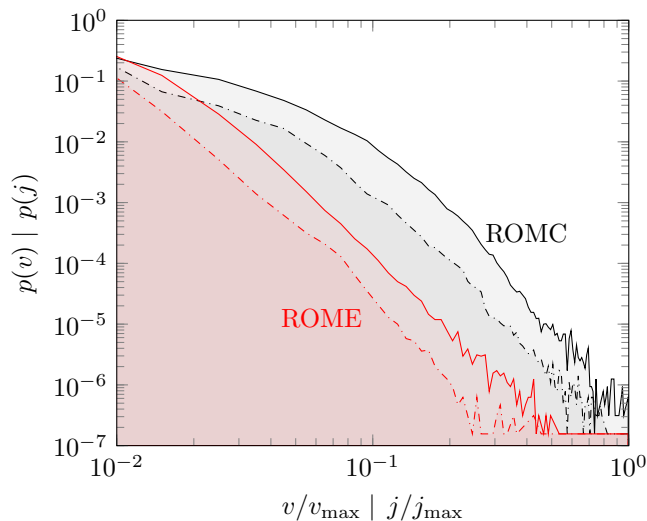
FIG. 8. (Color online) Comparison of velocity magnitude distribution $p(v)$ (solid) and current magnitude distribution $p(j)$ (dashed) in ROMC (black) and ROME (red) structures shown in Fig. 6. Both distributions, i.e., $p(v)$ and $p(j)$, follow similar trends, however the velocity decays with a significantly faster amplitude.

not independent [52, 53]. The amplitudes of the scaling relations are in general not known analytically. Therefore, we analyze the scaling behavior of the Euler characteristic numerically.

First, we calculate $(1 - \chi_o)/N$ for ROMR structures in dependence of the rescaled porosity. Calculations are performed for system sizes $L = 10a, 20a, 50a, 100a$ where a is the length of the long side of the rectangles. The simulations are repeated for different aspect ratios $1 : 1$, $1 : 2$, $1 : 4$ and $1 : 10$. An ensemble of 2500 samples for the smallest and 6 samples for the largest system size was simulated, which, except for the largest system size, results in an negligible error of the mean for all data points. As shown in the resulting curves in Fig. 9(a)-(d), we observe for all systems two distinct regimes with significantly different ϕ dependence. First, a critical regime close to ϕ_c and second, an effective medium regime where the data points collapse for different aspect ratios, but a significantly different slope of the curve compared to the critical regime is observed. No qualitative change in this behavior is observed for different system sizes. However, due to the rather limited system size of the ROMR structures, it is not obvious whether these two regimes persist for infinite system size.

Therefore, we also simulate site percolation on a 2D square lattice, for which a linear system size of $L = 2^{14}$ lattice sites can be achieved with an ensemble of 2^6 realizations and up to 2^{16} for the smallest system size $L = 2^5$. Here, N must be replaced by $(1 - p) \cdot L^2$, which, p is the probability that a site is conducting, corresponds to the volume occupied by obstacles. In this system, as shown in Fig. 9(e), we find extacly the same behavior as for

ROMR structures, for all system sizes. This further supports our assumption that the occurrence of two scaling regimes persists for other grain shapes and larger system sizes.

However, a direct determination of the scaling exponent from finite-size system simulations is not feasible [26]. Instead, an established method to extract critical exponents numerically is used from finite-size scaling [25, 26]. Here, we only give a brief description of the method: If we combine Eq. (4) and Eq. (17), we get $(1 - \chi_o)/N \propto (\phi - \phi_c)^\beta$, where $\beta = \mu/\alpha$. Because the correlation length ξ diverges at ϕ_c according to a power-law, we can use that $\xi \propto (\phi - \phi_c)^{-\nu}$ to obtain $(1 - \chi_o)/N \propto \xi^{-\beta/\nu}$. Since ξ is infinite at $\phi = \phi_c$, L becomes the confining length scale of the system and we obtain $(1 - \chi_o)/N \propto L^{-\beta/\nu}$. This assumption is now tested numerically. Here, our results might differ for site percolation (Fig. 9(e)) and ROMR structures (Fig. 9(f)). For site percolation we clearly observe a power-law with an exponent of $-\beta/\nu = -5/48$ in perfect agreement with percolation theory. This suggests that $\beta = 5/36$ indeed describes the scaling of the open Euler characteristic. However for ROMR structures the slope of the curve is significantly different for small L and only at large L becomes consistent with a scaling of $L^{-\beta/\nu}$ (see dashed line). Apparently the ROMR system is more sensitive to finite-size effects. However, larger L are computationally too expensive, so that $L < 256$ for square grains and worse for larger aspect ratios, since the amount of grains at a fixed ϕ diverges with the aspect ratio.

Nevertheless, our numerical results support the following interpretation: When we connect the scaling of the open Euler characteristic to the experimental observation the critical exponent seems to be irrelevant with respect to our experimental system sizes. In the critical regime from Eq. (4) percolation theory would yield

$$k \propto \left(\frac{1 - \chi_o}{N}\right)^{\mu/\beta} \tag{23}$$

which we obviously do not observe in the experiment. Instead our interpretation is that the power-law from Eq. (17) is related to the effective regime. Since in this regime the open Euler characteristic collapses, we argue that the same should be true for conductivity and permeability, however with a significantly different exponent (compared to β) with a value close to 1. A more detailed analysis of this problem, however, requires either new simulation or experimental studies of conductivity or permeability of structures with much larger system size. Consequently, a significant improvement of the computational and/or experimental effort is required. So far, only 20 structures could be measured and simulated. For a higher amount of samples a reliable automation of the experiment would be required. For large structures close to ϕ_c the resolution of the experiment must be improved by at least one order of magnitude. The same is true for the computational time required to solve the conductivity or permeability problem.
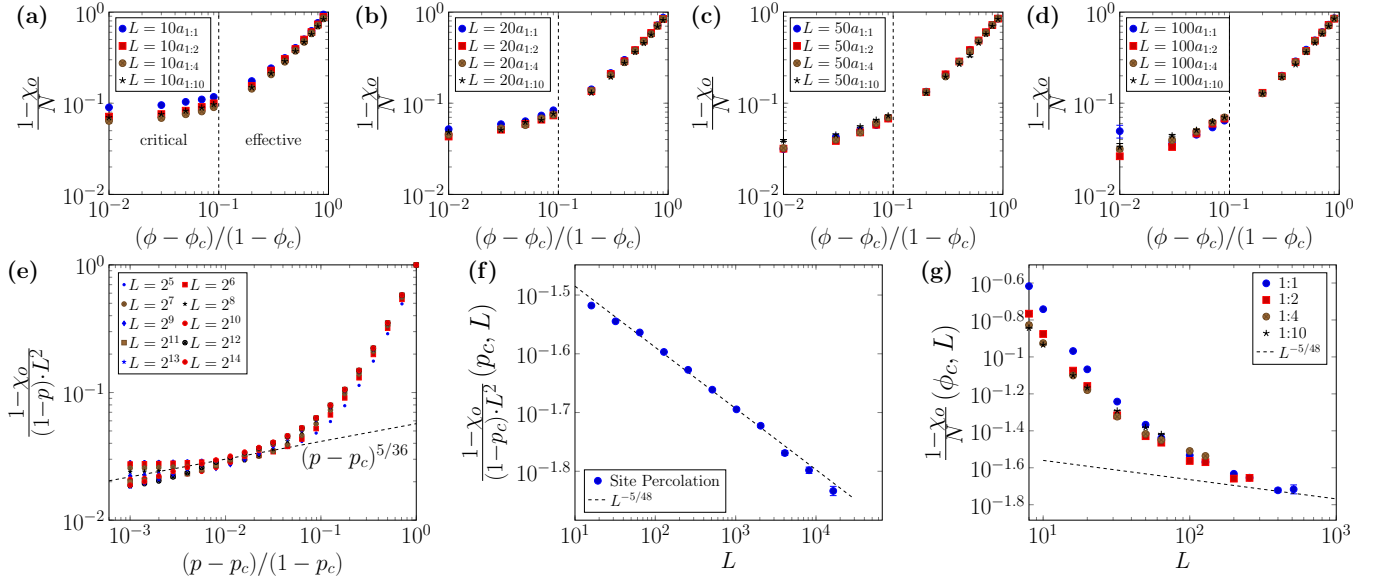
FIG. 9. Behavior of the Euler characteristic of the percolating cluster χ_o for **(a)-(d)** void percolation of different ROMR systems (aspect ratios $1:1$, $1:2$, $1:4$, $1:10$) as a function of the porosity ϕ and **(e)** site percolation on a 2D lattice function of the occupation probability p. For the ROMR structures system sizes of $L = 10a$, $20a$, $50a$ and $100a$ have been simulated. For site percolation $L = 2^2, ..., 2^{14}$. **(f)** Finite-size scaling analysis of χ_o for site percolation at the percolation threshold for difference linear system size L. **(g)** Finite-size scaling of χ_o in dependence of the linear system size L for ROMR structures.

X. SUMMARY

We have analyzed the permeability and conductivity of porous micro-models composed of randomly overlapping grains (Boolean models). We have analyzed void and grain percolation for overlapping circles and ellipses (i.e. structures where the void is conductive and structures where the grains are conductive). In all cases the relation between permeability and conductivity is well predicted by the Katz-Thompson model. In the case of void percolation the permeability can be deduced from the Euler characteristic of the percolating cluster normalized to the total number of grains, which required *a priori* knowledge of the grain density. For grain percolation a similar approach is studied based on the definition of an effective grain number $\hat{N}$, which is calculated from the global Minkowski functionals of the structures. This approach works qualitatively for ROME structures, but overestimates k for ROMC structures, due to the sensitivity of $\hat{N}$ on the occurrence of isolated pixels, which otherwise do not strongly affect k. For void percolation in the low grain-density limit it can be analytically shown that the formation factor is given by the Euler characteristic. The critical behavior of the Euler characteristic of the percolation cluster χ_o for $\phi \to \phi_c$ is analyzed numer-

ically to link our results to percolation theory. For the 2D square lattice, we find that χ_o scales with the critical exponent β only very close to ϕ_c. Further away from ϕ_c, an effective regime is found for both square lattice and Boolean models where the values of χ_o overlap for different systems, i.e. different grain shapes and system sizes, justifying the applicability of our model to many different types of structures.

A remaining question is the applicability to fully three-dimensional (3D) porous media. In principle 3D models are accessible experimentally, e.g. via 3D printing, and have also been studied numerically [54]. Also MFs are well understood in the 3D case, e.g. the Euler characteristic also vanishes close to ϕ_c. Therefore, it is reasonable to assume that Eq. (17) could hold in 3D, even though there is no intuitive interpretation similar to the 2D case. It must be expected however, that measurements and simulations are significantly more challenging and computationally more expensive.

[1] Committee on Chemical Engineering Frontiers: Research Needs and Opportunities, National Research Council,

Frontiers in Chemical Engineering: Research Needs and Opportunities (The National Academies Press, 1988).

[2] M. Sahimi, Rev. Mod. Phys. **65**, 1393 (1993).

[3] J. Bear, *Dynamics of fluids in porous media* (Dover Publications, 2013).

[4] S. Torquato, Appl. Mech. Rev. **44**, 37 (1991).

[5] C. H. Arns, M. A. Knackstedt, and K. R. Mecke, Phys. Rev. Lett. **91**, 215506 (2003).

[6] K. Mecke and C. H. Arns, J. Phys.: Condens. Matter **17**, S503 (2005).

[7] C. Scholz, F. Wirner, J. Götz, U. Rüde, G. E. Schröder-Turk, K. Mecke, and C. Bechinger, Phys. Rev. Lett. **109**, 264504 (2012).

[8] P. Lehmann, M. Berchtold, B. Ahrenholz, J. Tölke, A. Kästner, M. Krafczyk, H. Flühler, and H. Künsch, Adv. Water Resour. **31**, 1188 (2008).

[9] S. Yang, M. Liang, B. Yu, and M. Zou, Microfluid. Nanofluid. , 1 (2014).

[10] J. Kozeny, Sitzber. Akad. Wiss. Wien, Math-naturw **136**, Abt. II a, P. 277 (1927).

[11] A. J. Katz and A. H. Thompson, Phys. Rev. B **34**, 8179 (1986).

[12] P. N. Sen, J. N. Roberts, and B. I. Halperin, Phys. Rev. B **32**, 3306 (1985).

[13] A. Bunde, H. Harder, and S. Havlin, Phys. Rev. B **34**, 3540 (1986).

[14] M. Octavio, A. Octavio, J. Aponte, R. Medina, and C. J. Lobb, Phys. Rev. B **37**, 9292 (1988).

[15] N. Martys and E. J. Garboczi, Phys. Rev. B **46**, 6080 (1992).

[16] C. H. Arns, M. A. Knackstedt, and N. S. Martys, Phys. Rev. E **72**, 046304 (2005).

[17] J. R. Quispe, R. E. Rozas, and P. G. Toledo, Chem. Eng. J. **111**, 225 (2005).

[18] L. Andersson, A. C. Jones, M. A. Knackstedt, and L. Bergström, Acta Materialia **59**, 1239 (2011).

[19] Y.-B. Yi and A. M. Sastry, Phys. Rev. E **66**, 066130 (2002).

[20] J. A. Quintanilla and R. M. Ziff, Phys. Rev. E **76**, 051115 (2007).

[21] S. Kirkpatrick, Rev. Mod. Phys. **45**, 574 (1973).

[22] M. Sahimi, B. D. Hughes, L. E. Scriven, and H. T. Davis, Journal of Physics C: Solid State Physics **16**, L521 (1983).

[23] J. Tobochnik, D. Laing, and G. Wilson, Phys. Rev. A **41**, 3052 (1990).

[24] P. Grassberger, Physica A: Statistical Mechanics and its Applications **262**, 251 (1999).

[25] D. Stauffer and A. Aharony, *Introduction to percolation theory* (CRC press, 1994).

[26] K. Christensen and N. R. Moloney, *Complexity and criticality*, Vol. 1 (Imperial College Press, 2005).

[27] S. R. Quake and A. Scherer, Science **290**, 1536 (2000).

[28] G. Whitesides and A. Stroock, PHYSICS TODAY **54**, 42 (2001).

[29] J. C. Crocker and D. G. Grier, J. Colloid Interf. Sci. **179**, 298 (1996).

[30] J. G. Santiago, S. T. Wereley, C. D. Meinhart, D. J. Beebe, and R. J. Adrian, Exp. Fluids **25**, 316 (1998).

[31] R. Lindken, M. Rossi, S. Große, and J. Westerweel, Lab Chip **9**, 2551 (2009).

[32] M. Auset and A. A. Keller, Water Resour. Res. **40**, W03503 (2004).

[33] M. Auset and A. A. Keller, Water Resour. Res. **42**, W12S02 (2006).

[34] C. Scholz, F. Wirner, Y. Li, and C. Bechinger, Exp. Fluids **53**, 1327 (2012).

[35] D. Frenkel, Physica A: Statistical Mechanics and its Applications **313**, 1 (2002).

[36] M. E. Staben, A. Z. Zinchenko, and R. H. Davis, Phys. Fluids **15**, 1711 (2003).

[37] C. Pozrikidis, J. Fluid Mech. **261**, 199 (1994).

[38] H. Bruus, *Theoretical Microfluidics* (Oxford University Press, 2007).

[39] S. N. Chiu, D. Stoyan, W. S. Kendall, and J. Mecke, *Stochastic geometry and its applications* (John Wiley & Sons, 2013).

[40] M. Spanner, S. K. Schnyder, F. Höfling, T. Voigtmann, and T. Franosch, Soft Matter **9**, 1604 (2013).

[41] S. K. Schnyder, M. Spanner, F. Höfling, T. Franosch, and J. Horbach, Soft matter **11**, 701 (2015).

[42] K. Mecke and H. Wagner, J. Stat. Phys. **64**, 843 (1991).

[43] K. Mecke, T. Buchert, and H. Wagner, A&A **288**, 697 (1994).

[44] D. A. Klain and G.-C. Rota, *Introduction to geometric probability*, 1st ed. (Cambridge University Press, Cambridge, 1997) pp. XIV, 178 S.

[45] H. Mantz, K. Jacobs, and K. Mecke, J. Stat. Mech.: Theory Exp. **2008**, P12015 (2008).

[46] G. E. Schröder-Turk, W. Mickel, S. C. Kapfer, M. A. Klatt, F. M. Schaller, M. J. F. Hoffmann, N. Kleppmann, P. Armstrong, A. Inayat, D. Hug, *et al.*, Adv. Mater. **23**, 2535 (2011).

[47] G. E. Schröder-Turk, W. Mickel, S. C. Kapfer, F. M. Schaller, B. Breidenbach, D. Hug, and K. Mecke, New J. Phys. **15**, 083028 (2013).

[48] M. Hilpert and C. T. Miller, Adv. Water Resour. **24**, 243 (2001).

[49] W. Mickel, S. Münster, L. M. Jawerth, D. A. Vader, D. A. Weitz, A. P. Sheppard, K. Mecke, B. Fabry, and G. Schröder-Turk, Biophys. J. **95**, 6072 (2008).

[50] J. Andrade Jr, M. Almeida, J. Mendes Filho, S. Havlin, B. Suki, and H. Stanley, Phys. Rev. Lett. **79**, 3901 (1997).

[51] W. Xia and M. F. Thorpe, Phys. Rev. A **38**, 2650 (1988).

[52] K. R. Mecke, in *Statistical Physics and Spatial Statistics* (Springer, 2000) pp. 111–184.

[53] P. Schönhöfer and K. Mecke, in *Fractal Geometry and Stochastics V* (Springer, 2015) pp. 39–52.

[54] G. G. Pereira, P. M. Dupuy, P. W. Cleary, and G. W. Delaney, Prog. Comput. Fluid Dy. **12**, 176 (2012).

TABLE I. Table of properties of the analysed structures, corresponding the Boolean models of randomly overlapping circles and ellipses: Number of grains N, porosity ϕ, open porosity ϕ_o, total perimeter of the vectorized image S, perimeter of the open cluster S_o, perimeter of the pixelized image S_0, perimeter of the open cluster S_{d8}, Euler-characteristic of the vectorized image χ, Euler characteristic of percolation cluster χ_o, Euler-characteristic assuming 8-point connectivity χ_{d8}, cirtical pore diameter in 2D D_c, critical pore diameter in 3D l_c, effective number of grains calculated from inverting Minkowski functionals of the vectorized image $N_{\mathbf{eff}}$ and the pixelized image $N_{\mathbf{eff}d8}$, reconstructed number of grains $N_{\mathbf{rec}8}$ from inversion of the Minkowski functionals of the grain phase (equals $N_{\mathbf{eff}d8}$ for S1 − S10), permeability $k_{\mathbf{sim}}/cl_c{}^2$ from LB simulations, conductivity σ/σ_0 from FEM simulations.

Structure	N	ϕ	ϕ_o	S	S_o	S_{d8}	χ	χ_o	χ_{d8}	D_c	l_c	$N_{\mathbf{eff}}$	$N_{\mathbf{eff}d8}$	$N_{\mathbf{rec}8}$	$k_{\mathbf{exp}}/cl_c^2$	$k_{\mathbf{sim}}/cl_c^2$	σ/σ_0
S1	4592	0.365	0.298	367820	281380	444740	167	-220(d4)	195	2.421	2.421	4593	5472	5472	0.0158	0.0273	0.0118
S2	3968	0.418	0.401	365637	337516	444361	-81	-395(d4)	-53	11.506	∞	3999	4697	4697	0.047	0.0414	0.0764
S3	2704	0.551	0.549	326905	321646	401440	-442	-635(d4)	-416	21.984	∞	2553	2894	2894	0.137	0.1575	0.2107
S4	1632	0.701	0.700	249486	248098	313041	-628	-724(d4)	-607	51.306	∞	1496	1668	1668	0.385	0.3807	0.4405
S5	754	0.850	0.850	137404	137123	180900	-485	-520(d4)	-474	100.018	∞	688	740	740	0.641	0.6653	0.7031
S6	2064	0.651	0.266	508418	169009	614682	664	-45(d4)	704	5.957	5.957	2014	2474	2474	0.00696	0.0112	0.00851
S7	2176	0.639	0.400	522543	271616	631363	751	-80(d4)	790	6.245	6.245	2151	2659	2659	0.02	0.0174	0.0135
S8	1840	0.684	0.549	474276	332151	577379	463	-146(d4)	500	6.275	6.275	1714	2108	2108	0.0385	0.0355	0.0392
S9	1387	0.751	0.700	391959	336787	479984	54	-275(d4)	86	41.254	∞	1283	1511	1511	0.118	0.1193	0.1501
S10	771	0.854	0.850	247904	241577	313061	-250	-352(d4)	-231	67.429	∞	712	805	805	0.3598	0.3333	0.3787
S11	5017	0.668	0.278	368788	142102	451433	-688	-378	-660	5.85	5.85	2547	2833	5457	0.016	0.019	0.01228
S12	4835	0.658	0.400	367009	211801	450170	-680	-574	-653	10.72	∞	2579	2880	5075	0.0228	0.021	0.02602
S13	5273	0.682	0.550	356548	274552	438116	-774	-791	-745	6.05	6.05	2496	2761	5289	0.040	0.034	0.03498
S14	6174	0.742	0.700	346916	317436	428861	-1122	-1179	-1095	35.93	∞	2600	2833	6888	0.210	0.132	0.16322
S15	8726	0.851	0.850	278084	276830	350582	-1834	-1842	-1814	47.97	∞	2685	2829	10284	0.304	0.425	0.47783
S16	2405	0.388	0.270	544241	370891	665501	-1406	-1114	-1363	13.73	∞	13382	15816	2481	0.01106	0.017	0.0227
S17	2602	0.417	0.400	569519	541621	697969	-1793	-1808	-1752	12.91	∞	13586	15988	2691	0.04366	0.049	0.0636
S18	3882	0.551	0.549	644938	641737	800403	-3865	-3881	-3819	18.29	∞	13811	15873	4154	0.0964	0.131	0.1724
S19	5822	0.701	0.700	647728	647728	815653	-6338	-6348	-6290	21.54	∞	13310	14816	8698	0.186	0.297	0.3779
S20	9095	0.850	0.850	504371	504372	652581	-8655	-8657	-8617	27.66	∞	11941	12756	18708	0.7416	0.536	0.6388